

STRUCTURAL – ELECTRONIC PROPERTIES CORRELATION OF
CdSe QUANTUM DOT SOLAR CELL USING EXPERIMENTAL
AND THEORETICAL INVESTIGATIONS

SAIFFUL KAMALUDDIN BIN MUZAKIR @ LOKMAN @ HJ ARSHAD

Thesis submitted in fulfilment of the requirements
for the award of the degree of
Doctor of Philosophy (Advanced Materials)

Faculty of Industrial Sciences & Technology
UNIVERSITI MALAYSIA PAHANG

MARCH 2015

ABSTRACT

Solar cells are in focus for decades due to their capability to convert solar energy into electrical energy. Quantum dots sensitized solar cell (QDSC), in which the photovoltaic (PV) effect occurs at the interface between a quantum dot (QD) conjugated wide band gap metal oxide semiconductor (MOS) and a redox electrolyte, gained much consideration due to their relatively simpler device structure and similarity to dye sensitized solar cell (DSSC), in which dye molecules replace QDs. The QDs are potentially having larger absorption cross-section, tuneable band edges, and atomic-like energy levels. These salient features make QDs capable of delivering more than one electron per single absorbed photon of sufficient energy, a phenomenon known as multi-exciton generation (MEG). The MEG effect makes QDSCs capable of achieving PV conversion efficiency (PCE) as high as 60% theoretically. Despite the remarkable feature of QDs as a light absorber, QDSCs deliver much inferior practical PCE (~8.6 %). Besides, they show inferior PCE compared to DSSCs (~13%). Therefore, this doctoral research aims to establish the structure-property correlation in QDSCs. A combination of experimental results and quantum chemical calculations under the framework of density functional theory (DFT) was employed for this purpose. In this approach, firstly CdSe QDs were synthesized using chemical methods and studied their structure and properties. Secondly realistic cluster models were empirically developed using DFT and experimental results. The structure-property correlation was established by comparing the experimental and theoretical results. The calculated absorption cross-section, band edges, band gaps, and emitting states of QDs with and without surface ligands were compared with that of $\text{RuL}_2(\text{NCS})_2 \cdot 2\text{H}_2\text{O}$; $L = 2,2'$ -bipyridyl-4,4'-dicarboxylic acid (N3) dye to correlate the capability of light absorption of QDs or dye molecules on the overall performance of device. This procedure was adopted to (i) understand the fundamental differences of electronic states in the bare QDs and the dye structures and (ii) evaluate electron channelling in QDs-ligand conjugate thus correlating with electron injection efficiency from QDs to MOS. Five parameters were concluded to have distinct effects on the PV properties of QDSCs. They are (i) emitting states of QDs, (ii) ligand usage, (iii) QDs size distribution, (iv) absorption cross-section, and (v) redox potential of electrolyte. The QDs-MOS conjugates were chemically developed and spectroscopically demonstrated efficient electron injection from QDs to MOS. However, such structures raised serious concerns on long term stability under operating conditions. This thesis finally propose future possible methodologies for stable and efficient QDSCs.

ABSTRAK

Sel suria menjadi fokus semenjak beberapa dekad kerana keupayaannya untuk menukar tenaga suria kepada tenaga elektrik. Sel suria terpeka titik kuantum (QDSC), dengan kesan fotovoltaiik (PV) berlaku di antara permukaan konjugat titik kuantum (QD)–semikonduktor logam oksida berjurang tenaga lebar (MOS) dan elektrolit, menerima pertimbangan yang sewajarnya berikutan struktur peranti yang mudah dan persamaan dengan sel suria terpeka pewarna (DSSC), dengan molekul pewarna menggantikan titik kuantum (QD). QD berpotensi untuk mempunyai keratan rentas spektrum serapan yang luas, mengubah jurang tenaga and ciri tahap tenaga seperti atom. Ciri-ciri penting ini menjadikan QD mampu mengujakan lebih dari satu elektron dengan setiap penyerapan satu foton dengan tenaga yang mencukupi. Fenomena tersebut dinamakan penjanaan multieksiton (MEG) yang menjadikan QDSC mampu mencapai kecekapan penukaran tenaga foto (PCE) secara teorinya sehingga 60%. Namun, walaupun dengan adanya ciri-ciri luar biasa ini, penggunaan QD sebagai penyerap cahaya peranti QDSC hanya mampu menghasilkan PCE yang rendah secara praktikal (~8.6%). Tambahan pula, kecekapan tersebut lebih rendah berbanding dengan kecekapan DSSC (~13%). Oleh itu, kajian peringkat kedoktoran ini menyasarkan pembuktian korelasi di antara struktur komponen dan ciri fotovoltaiik QDSC. Gabungan keputusan ujikaji dan pengiraan peringkat kimia kuantum menggunakan teori ketumpatan fungsian (DFT) telah digunakan untuk tujuan ini. Melalui pendekatan ini, pertama sekali QD CdSe telah disintesis menggunakan kaedah kimia dan struktur serta ciri-cirinya dikaji. Kedua, model kluster realistik dibangunkan secara empirik menggunakan DFT dan keputusan ujikaji. Korelasi struktur-ciri dibuktikan dengan melakukan perbandingan di antara keputusan ujikaji dan pengiraan teori. Ciri-ciri QD dan konjugat QD–ligan seperti keratan rentas spektrum penyerapan, aras tenaga, jurang tenaga dan keadaan teruja telah dibandingkan dengan ciri-ciri yang dimiliki oleh asid $\text{RuL}_2(\text{NCS})_2 \cdot 2\text{H}_2\text{O}$; $L = 2,2'$ –bipyridyl-4,4'-dicarboxylic (pewarna N3) untuk pembuktian korelasi di antara keupayaan penyerapan cahaya oleh QD dan molekul pewarna dengan prestasi keseluruhan peranti. Prosedur ini dijalankan untuk (i) memahami perbezaan keadaan elektronik kluster-kluster QD dan molekul pewarna secara asas dan (ii) menilai kecekapan penyaluran elektron di dalam konjugat QD–ligan yang berkait rapat dengan kecekapan suntikan elektron dari QD kepada MOS. Sebagai kesimpulan, lima parameter mempunyai kesan kepada ciri PV QDSC iaitu, (i) keadaan tersinar QD, (ii) penggunaan ligan, (iii) taburan saiz QD, (iv) luas keratan rentas spektrum penyerapan dan (v) potensi redoks elektrolit. Konjugat QD-MOS telah dihasilkan secara kimia dan menunjukkan kecekapan suntikan elektron dari QD ke MOS secara spektroskopik. Walaubagaimanapun, struktur-struktur ini telah menimbulkan kebimbangan terhadap kestabilan jangka panjang pengoperasian peranti. Tesis ini mencadangkan metodologi yang mungkin boleh digunakan untuk menghasilkan QDSC yang stabil dan cekap.

TABLE OF CONTENTS

| | Page |
|--------------------------------------|-------------|
| TITLE PAGE | i |
| STATEMENT OF AWARD FOR DEGREE | ii |
| SUPERVISOR’S DECLARATION | iii |
| STUDENT’S DECLARATION | iv |
| DEDICATION | v |
| ACKNOWLEDGEMENTS | vi |
| ABSTRACT | vii |
| ABSTRAK | viii |
| TABLE OF CONTENTS | ix |
| LIST OF TABLES | xiv |
| LIST OF FIGURES | xix |
| LIST OF SYMBOLS | xxxv |
| LIST OF ABBREVIATIONS | xxxviii |

CHAPTER 1 INTRODUCTION

| | | |
|-----|--------------------------|---|
| 1.1 | Background | 1 |
| 1.2 | Problem Statement | 3 |
| 1.3 | Objectives | 4 |
| 1.4 | Scope of Research | 4 |
| 1.5 | Overview of the Thesis | 6 |
| 1.6 | Prime Novelty Statements | 7 |

CHAPTER 2 LITERATURE REVIEW

| | | |
|-----|---|----|
| 2.1 | Introduction | 8 |
| 2.2 | Classification of Solar Cells and Device Structures | 8 |
| | 2.2.1 Crystalline Solar Cell | 9 |
| | 2.2.2 Thin Film Solar Cell | 10 |
| | 2.2.3 Molecular Absorber Solar Cell | 13 |

| | | |
|-------|--|----|
| 2.3 | Limitation of Bulk Semiconductor-Based Solar Cell | 17 |
| 2.3.1 | Thermalization of Excited State Electron | 17 |
| 2.3.2 | Theoretical Maximum Efficiency (~32%) of <i>p-n</i> Junction Solar Cells | 18 |
| 2.3.3 | Breaking the Theoretical Maximum Efficiency | 18 |
| 2.4 | Superior Properties of Quantum Dots for Quantum Dots Solar Cell Applications | 19 |
| 2.4.1 | Multi Exciton Generation (MEG) | 19 |
| 2.4.2 | Advantages of QDs over Organic and Organometallic Fluorophores (Dye) | 19 |
| 2.4.3 | Performance of DSSCs Exceeding That of the QDSCs | 20 |
| 2.5 | Advancement in Quantum Dots Solar Cells Research | 20 |
| 2.6 | DFT | 31 |
| 2.7 | Critical Area of Study | 35 |

CHAPTER 3 MATERIALS AND METHOD

| | | |
|-------|---|----|
| 3.1 | Research Methodology | 39 |
| 3.2 | CdSe Quantum Dots Synthesis and Characterization | 41 |
| 3.2.1 | Microemulsion Synthesis Procedure | 41 |
| 3.2.2 | Colloidal Organometallic Synthesis and QDs Extraction Procedure | 42 |
| 3.2.3 | CdSe Quantum Dots Characterization | 43 |
| 3.3 | Instrument and Tools Used | 43 |
| 3.3.1 | X-ray Diffractometer (XRD) | 43 |
| 3.3.2 | Field Emission Electron Microscope (FESEM) | 44 |
| 3.3.3 | Transmission Electron Microscope (TEM) | 45 |
| 3.3.4 | Selected Area Electron Diffraction (SAED) | 46 |
| 3.3.5 | UV-Visible Spectrometer | 47 |
| 3.3.6 | Photoluminescence Spectrometer | 48 |
| 3.3.7 | Fourier Transform Infrared (FTIR) Spectroscopy | 50 |
| 3.4 | CdSe Quantum Dots Cluster Modelling | 50 |
| 3.4.1 | Procedure of Realistic Cluster Modelling | 50 |
| 3.4.3 | Z-matrix Preparations | 53 |
| 3.5 | TiO ₂ Coating on Conducting Glass Procedure | 54 |
| 3.5.1 | TiO ₂ Layer Deposition using Commercial Solaronix Ti-Nanoxide T/SP | 54 |
| 3.5.2 | TiO ₂ Nanorods Preparation using Hydrothermal Procedure | 54 |

| | | |
|-------|---|----|
| 3.6 | CdSe QDs–TiO ₂ Conjugation Procedure | 55 |
| 3.6.1 | Direct Attachment and Ligand Assisted Procedure | 55 |
| 3.6.2 | Successive Ionic Liquid Adsorption and Reaction (SILAR) Procedure | 55 |
| 3.6.3 | Room Temperature Organometallic Procedure | 56 |
| 3.6.4 | Low Temperature Chemical Bath Deposition (CBD) Procedure | 56 |
| 3.7 | Electron Injection Efficiency Study | 56 |
| 3.8 | Softwares for Simulations and Data Analysis | 56 |

CHAPTER 4 IDENTIFICATION AND REALISTIC CLUSTER MODEL VALIDATION

| | | |
|-------|---|----|
| 4.1 | Introduction | 58 |
| 4.2 | Identification of CdSe Quantum Dots Under Microemulsion Procedure | 59 |
| 4.2.1 | Procedure | 59 |
| 4.2.2 | Temporal Evolution of QDs Size and Photoluminescence Properties | 60 |
| 4.2.3 | Extraction of CdSe QDs from Microemulsion Template | 63 |
| 4.3 | Identification of Cdse Quantum Dots under Room Temperature Colloidal Organometallic Procedure | 68 |
| 4.3.1 | Procedure | 68 |
| 4.3.2 | Temporal Evolution of QDs Size and Photoluminescence Properties | 69 |
| 4.3.3 | Extraction of CdSe QDs from Aliquots | 74 |
| 4.4 | Realistic Cluster Modelling of Quantum Dots | 75 |
| 4.4.1 | Procedure | 75 |
| 4.4.2 | Geometry Optimization of CdSe QDs | 77 |
| 4.4.3 | Vibrational Frequency Calculations of QDs Cluster | 79 |
| 4.4.4 | Excitation Energies, Oscillator Strength Calculations, HOMO-LUMO Transition and Comparison with Experimental Result | 80 |
| 4.4.5 | Bandgap Estimation of QDs Cluster | 83 |
| 4.4.6 | Geometry of Calculated QDs Cluster | 84 |
| 4.5 | Realistic Cluster Modelling of N3 Dye Molecule | 87 |
| 4.6 | Realistic Cluster Modelling of Ligand Molecules | 89 |
| 4.7 | Realistic Cluster Modelling of QDs-Ligand Conjugate | 92 |
| 4.8 | Conclusions | 94 |

CHAPTER 5 EFFECT OF EMITTING STATES OF CdSe QUANTUM DOTS AND QUANTUM DOTS–LIGAND CONJUGATES ON THE CHARGE INJECTION DYNAMICS OF QUANTUM DOTS SOLAR CELLS

| | | |
|---------|---|-----|
| 5.1 | Introduction | 95 |
| 5.2 | DSSCs vs QDSCs Device Structure Comparison | 95 |
| 5.3 | Emitting State Properties of CdSe QDs, N3 Dye Molecule and QDs – Ligand Conjugate | 97 |
| 5.3.1 | Absorption Cross-Section Comparison of CdSe QDs and N3 Dye Molecule | 97 |
| 5.3.2 | Affecting Factors of Injection Efficiency in CdSe-based QDSC | 99 |
| 5.3.2.1 | The effect of CdSe QDs size distribution | 100 |
| 5.3.2.2 | The effect of electron density of different size of QDs | 102 |
| 5.3.2.3 | The effect of ligand usage | 106 |
| 5.3.3 | Fluorophore Reduction Efficiency (δ_{DR}) | 110 |
| 5.4 | Conclusions | 114 |

CHAPTER 6 SPECTROSCOPIC PROPERTIES OF CdSe QDs–TiO₂ CONJUGATES

| | | |
|-------|---|-----|
| 6.1 | Introduction | 115 |
| 6.2 | Ligand Assisted and Direct Attachment Procedure | 117 |
| 6.3 | Successive Ionic Liquid Adsorption and Reaction (SILAR) Procedure | 120 |
| 6.4 | Room Temperature Organometallic Procedure | 124 |
| 6.4.1 | Spectroscopic Properties of 4 Hours Immersed TiO ₂ -FTO | 126 |
| 6.4.2 | Spectroscopic Properties of 24 Hours Immersed TiO ₂ -FTO | 128 |
| 6.4.3 | Spectroscopic Properties of 168 Hours Immersed TiO ₂ - FTO | 130 |
| 6.5 | Chemical Bath Deposition (CBD) for 24 Hours at 2 °C | 132 |
| 6.6 | Hindrances of QDs – TiO ₂ Conjugation for Quantum Dots Solar Cells Application | 134 |
| 6.6.1 | Size Dependent Electron Injection Efficiency | 134 |
| 6.6.2 | Small Amount of Growth of Targeted Size of QDs in Organometallic Procedure | 134 |

| | | |
|-------|---|-----|
| 6.6.3 | Instability of Small QD – TNRs Conjugate Upon Exposure to Air | 134 |
| 6.6.4 | Energy Level Misalignment Issue of Ligand | 135 |
| 6.6.5 | Low QDs Adsorption in DA Procedure | 135 |
| 6.6.6 | Prospect of SILAR Procedure | 135 |

CHAPTER 7 CONCLUSIONS AND RECOMMENDATIONS

| | | |
|-----|--------------------------------|-----|
| 7.1 | Conclusions | 137 |
| 7.2 | Recommendations of Future Work | 140 |

| | |
|-------------------|-----|
| REFERENCES | 141 |
|-------------------|-----|

APPENDICES

| | | |
|---|---|-----|
| A | Microemulsion Region Determinations using Polarized Optical Microscope and Conductivity Meter | 155 |
| B | Fitted Experimental Absorption Spectra for Four Excitonic Peaks Assignment (Microemulsion-Based QDs) | 159 |
| C | Fitted Experimental Absorption Spectra for Four Excitonic Peaks Assignment (Organometallic-Based QDs) | 167 |
| D | Internal Coordinate Specification of Quantum Dots for Geometry Optimization | 170 |
| E | Infrared Spectra of The Optimized Geometries of CdSe Quantum Dots | 183 |
| F | Convergence Failure of Proposed QDs Structure | 202 |
| G | Optimization Paramaters of $\text{RuL}_2(\text{NCS})_2 \cdot 2\text{H}_2\text{O}$; $L = 2,2'$ -bipyridyl-4,4'-dicarboxylic Acid (N3) Dye | 220 |
| H | Optimization Parameters of Ligand Molecules | 223 |
| I | Optimization Parameters of QD–Ligand Conjugate | 227 |
| J | Infrared Spectra of The Optimized Geometries of $(\text{CdSe})_{13}$ –Ligand Conjugates | 235 |
| K | Optimization Parameters of 1-butyl-3-methylimidazolium Iodide Ionic Liquid (IonLic BMII) | 247 |
| L | Realistic Model Validation of 1-butyl-3-methylimidazolium Iodide Ionic Liquid (IonLic BMII) | 249 |
| M | Redox Potential Calculations of 1-butyl-3-methylimidazolium Iodide Ionic Liquid (IonLic BMII) | 251 |
| N | Accolades | 254 |

LIST OF TABLES

| Table No. | Title | Page |
|------------------|---|-------------|
| 2.1 | Complete device structure of CdSe-based solar cells under 1 Sun illumination (AM1.5 G) from 1993-2014 | 25 |
| 3.1 | Z-matrix of basic hexagonal structure of CdSe | 51 |
| 3.2 | Number of optimization parameter pair for the lowest energy structure calculations | 51 |
| 3.3 | Convergence criteria of optimization of (CdSe) ₆ structure | 52 |
| 3.4 | Command lines used for DFT calculations | 52 |
| 4.1 | Properties of CdSe QDs synthesized at different reaction time | 60 |
| 4.2 | Absorption coefficient and bandgap of CdSe QDs synthesized at different reaction time | 60 |
| 4.3 | Properties of extracted CdSe QDs synthesized at different reaction time | 62 |
| 4.4 | Properties of CdSe QDs synthesized using organometallic procedure at different condition | 71 |
| 4.5 | Summary of calculated QDs clusters. The size of clusters was calculated based on the calculated volume of the optimized geometries | 81 |
| 4.6 | Minimum Cd–Se bond lengths of simulated QDs clusters; the numbers in parentheses give the percentage difference from that of the bulk CdSe | 82 |
| 5.1 | The calculated diameter, oscillator strengths at the first excitonic peak position of each fluorophore and absorption cross-section of (a) N3 dye, (b) (CdSe) ₆ , (c) (CdSe) ₁₃ , (d) (CdSe) ₁₆ , and (e) (CdSe) ₂₆ | 97 |
| 5.2 | The detail of calculated LUMO and HOMO energy levels of the QDs clusters | 100 |
| 5.3 | Summary of calculated HOMO, LUMO, band gap energies of the QDs, ligands and their adsorption conjugate with QDs | 106 |

| Table No. | Title | Page |
|------------------|---|-------------|
| 5.4 | Typical CdSe QDs-based and N3 dye-based solar cell device structures and parameters | 107 |
| 5.5 | Ligand chain length has significant effect on the adsorption energy; the shorter the length the higher would be the adsorption energy | 109 |
| 6.1 | PL intensity quenching of CdSe QD – TiO ₂ structure fabricated using different technique | 135 |
| A-1 | Conductivity measurements of microemulsion | 157 |
| D-1 | Optimization parameters for (CdSe) ₆ geometry optimization | 169 |
| D-2 | Bond lengths, bond angles and dihedral angles output of (CdSe) ₆ geometry optimization | 169 |
| D-3 | Optimization parameters for (CdSe) ₁₃ geometry optimization | 170 |
| D-4 | Bond lengths, bond angles and dihedral angles output of (CdSe) ₁₃ geometry optimization | 171 |
| D-5 | Optimization parameters for (CdSe) ₁₆ geometry optimization | 172 |
| D-6 | Bond lengths, bond angles and dihedral angles output of (CdSe) ₁₆ geometry optimization | 173 |
| D-7 | Optimization parameters for (CdSe) ₂₆ geometry optimization | 174 |
| D-8 | Bond lengths, bond angles and dihedral angles output of (CdSe) ₂₆ geometry optimization | 176 |
| D-9 | Optimization parameters for (CdSe) ₃₂ geometry optimization | 178 |
| D-10 | Bond lengths, bond angles and dihedral angles output of (CdSe) ₃₂ geometry optimization | 180 |
| E-1 | Calculated infrared spectrum data of (CdSe) ₆ structure | 181 |
| E-2 | Calculated infrared spectrum data of (CdSe) ₁₃ structure | 187 |
| E-3 | Calculated infrared spectrum data of (CdSe) ₁₆ structure | 191 |

| Table No. | Title | Page |
|------------------|---|-------------|
| E-4 | Calculated infrared spectrum data of (CdSe) ₂₆ structure | 194 |
| E-5 | Calculated infrared spectrum data of (CdSe) ₃₂ structure | 198 |
| F-1 | Proposed parameters for (CdSe) ₃₆ geometry optimization | 201 |
| F-2 | Proposed bond lengths, bond angles and dihedral angles for (CdSe) ₃₆ geometry optimization | 203 |
| F-3 | Proposed parameters for (CdSe) ₄₀ geometry optimization | 205 |
| F-4 | Proposed bond lengths, bond angles and dihedral angles for (CdSe) ₄₀ geometry optimization | 207 |
| F-5 | Proposed parameters for (CdSe) ₄₅ geometry optimization | 209 |
| F-6 | Proposed bond lengths, bond angles and dihedral angles for (CdSe) ₄₅ geometry optimization | 212 |
| F-7 | Proposed parameters for (CdSe) ₄₈ geometry optimization | 214 |
| F-8 | Proposed bond lengths, bond angles and dihedral angles for (CdSe) ₄₈ geometry optimization | 216 |
| G-1 | Proposed parameters for N3 dye molecule geometry optimization | 219 |
| G-2 | Optimized value of bond lengths, bond angles and dihedral angles for N3 dye molecule | 220 |
| H-1 | Optimization parameters for MAA geometry | 221 |
| H-2 | Optimized bond lengths, bond angles and dihedral angles of MAA geometry | 222 |
| H-3 | Optimization parameters for MPA geometry | 223 |
| H-4 | Optimized bond lengths, bond angles and dihedral angles of MPA geometry | 223 |
| H-5 | Optimization parameters for MSA geometry | 224 |

| Table No. | Title | Page |
|------------------|---|-------------|
| H-6 | Optimized bond lengths, bond angles and dihedral angles of MSA geometry | 224 |
| H-7 | Optimization parameters for MBA geometry | 225 |
| H-8 | Optimized bond lengths, bond angles and dihedral angles of MBA geometry | 225 |
| I-1 | Optimization parameters for (CdSe) ₁₃ -MAA geometry | 226 |
| I-2 | Optimized bond lengths, bond angles and dihedral angles of (CdSe) ₁₃ -MAA geometry | 227 |
| I-3 | Optimization parameters for (CdSe) ₁₃ -MPA geometry | 228 |
| I-4 | Optimized bond lengths, bond angles and dihedral angles of (CdSe) ₁₃ -MPA geometry | 229 |
| I-5 | Optimization parameters for (CdSe) ₁₃ -MSA geometry | 230 |
| I-6 | Optimized bond lengths, bond angles and dihedral angles of (CdSe) ₁₃ -MSA geometry | 231 |
| I-7 | Optimization parameters for (CdSe) ₁₃ -MBA geometry | 232 |
| I-8 | Optimized bond lengths, bond angles and dihedral angles of (CdSe) ₁₃ -MBA geometry | 233 |
| J-1 | Calculated infrared spectrum data of (CdSe) ₁₃ -MAA conjugate | 234 |
| J-2 | Calculated infrared spectrum data of (CdSe) ₁₃ -MBA conjugate | 237 |
| J-3 | Calculated infrared spectrum data of (CdSe) ₁₃ -MPA conjugate | 240 |
| J-4 | Calculated infrared spectrum data of (CdSe) ₁₃ -MSA conjugate | 241 |
| K-1 | Optimization parameters for IonLic BMII geometry | 246 |
| K-2 | Optimized bond lengths, bond angles and dihedral angles of IonLic BMII geometry | 247 |
| M-1 | Calculated parameters of anion state of IonLic BMII | 250 |

| Table No. | Title | Page |
|------------------|---|-------------|
| M-2 | Calculated parameters of neutral state of IonLic BMII | 250 |

LIST OF FIGURES

| Figure No. | Title | Page |
|------------|---|------|
| 1.1 | The series of events in the electron density of states (DoS) when a bulk semiconductor is reduced to the size of QDs | 2 |
| 1.2 | Energetic diagram of (a) thermalization in bulk structure and (b) multi-exciton generation (MEG) in quantum wells and dots | 3 |
| 2.1 | Classification of solar cells | 9 |
| 2.2 | Typical structure of crystalline Si solar cell. Electron-hole pairs are generated in the <i>p</i> -type Si, where electron diffuses towards <i>p-n</i> junction and drifts to the <i>n</i> -type layer | 10 |
| 2.3 | Schematic structure of <i>p-i-n</i> junction thin film <i>a</i> -Si:H solar cell. Electron-hole pairs are generated in the intrinsic layer; separated to the <i>n</i> -type and <i>p</i> -type Si. The refractive index, <i>n</i> is an approximate value for light trapping purposes | 11 |
| 2.4 | Low efficiency SWCNT-based solar cell | 12 |
| 2.5 | Typical perovskite solar cell composed of fluorine doped tin oxide (FTO) conducting glass, compact TiO ₂ (50 nm thickness), mesoporous TiO ₂ intruded with perovskite material (300 nm thickness) and hole transport material (600 nm thickness) | 13 |
| 2.6 | A typical DSSC device structure | 14 |
| 2.7 | (a) Bilayer organic solar cell device structure and (b) typical energy level alignment for efficient electron injection from D to A | 15 |
| 2.8 | (a) Device structure of bulk heterojunction solar cell and (b) cross-sectional morphology of the donor and acceptor network | 16 |
| 2.9 | Different type of QDs based molecular solar cells, (a) QDs/polymer BHJ, (b) Schottky junction solar cell and (c) QDSC. “e” and “h” denote the electron and hole generated upon absorption of photon with sufficient energy ($h\nu > \text{bandgap}$); separated to opposite direction | 16 |

| Figure No. | Title | Page |
|------------|---|------|
| 2.10 | Energetic diagram of (a) thermalization of photoexcited electron in bulk Si and (b) impact ionization in bulk Si upon absorption of high energy photon (i.e., > 3.6 bandgap) | 18 |
| 2.11 | Initiation of MEG process with (a) excitation of electron upon absorption of photon with energy $\gg E_g$, (b) relaxation of excited electron to LUMO and internal photon emissions ($h\nu > E_g$), (c) internal photon absorptions by ground state electron and extra exciton formations | 20 |
| 2.12 | The graph shows among the best CdSe-based solar cell efficiency (with recorded IPCE) in the corresponding year. The efficiency of photon conversion to charge (IPCE) is correlated to the power conversion efficiency (η) | 22 |
| 2.13 | The advancement of single crystal Si, DSSC and QDSC | 24 |
| 2.14 | The concept of DFT calculations | 31 |
| 2.15 | An illustration of electron and nucleus of hydrogen atom | 32 |
| 2.16 | The process flow of ground state energy calculation by (a) DFT calculations and (b) Schrodinger equation calculations route | 35 |
| 2.17 | The yielded incident photon to charge efficiency (boxes) and power conversion efficiency (circles) by fabricated cell using respective CdSe QDs size | 36 |
| 2.18 | (a) Optimized structure of N3 dye molecule and (b) excited state electron mapping generated by time dependent density functional theory (TDDFT). The distance between the nearest LUMO to the anchoring hydrogen at $-\text{COOH}$ functional group (indicated by circles) is correlated to charge injection efficiency from dye to MOS | 37 |
| 3.1 | Flow of research methodology | 40 |
| 3.2 | (a) Top and (b) side view of SAED pattern generation | 47 |

| Figure No. | Title | Page |
|-------------------|--|-------------|
| 3.3 | Jablonski diagram describing excitation of electron in HOMO-0 of a typical specimen to UMO, subsequent energy loss through phonon emissions that causes the electron to fall to LUMO+0. Photon is emitted via radiative recombination of electron from the LUMO+0 to HOMO-0 | 49 |
| 3.4 | User interface of Gaussian 09 W software that shows field for stating (a) the output and memory setting, (b) basis set and functional command line, (c) title of calculations, (d) charge and multiplicity of the optimized system and (e) z-matrix as input of lowest energy structure optimization | 53 |
| 3.5 | (a) Four atoms of mercaptosuccinic acid were chosen as an example, which were numbered accordingly, i.e., 5C, 3C, 2O and 1H (dashed circles). (b) Two planes of (i) 5C – 3C and (ii) 1H – 2O are connected at 2O – 3C bond. (c) Dihedral angle is the torsion angle between these two planes | 54 |
| 4.1 | (a) From left, Se and Cd precursor contained microemulsions and (b) the extracted CdSe QDs synthesized at different reaction time (from left 30, 60 and 120 minutes) | 58 |
| 4.2 | Temporal evolution of the first excitonic peak position within (a) 1, (b) 5, (c) 10, (d) 15, (e) 30, (f) 60 and (g) 120 minutes of reaction time | 59 |
| 4.3 | Temporal evolution of the photoluminescence property of CdSe synthesized in microemulsion template within (a) 1, (b) 5, (c) 10, (d) 15, (e) 30, (f) 60 and (g) 120 minutes of reaction time | 61 |
| 4.4 | FESEM micrographs of CdSe QDs at (a) 100 000 and (b) 300 000 times of magnification | 62 |
| 4.5 | HRTEM micrographs of CdSe QDs at (a) 88 000 and (b) 255 000 times of magnification | 63 |

| Figure No. | Title | Page |
|-------------------|---|-------------|
| 4.6 | (a) Broad XRD peaks of wurtzite CdSe QDs synthesized using microemulsion procedure extracted at 30 minutes of reaction time. (b) Sharp and distinct XRD peaks of wurtzite crystal were revealed upon precursors and concentration change. Vertical lines indicate the possible Bragg reflections (JCPDS-ICDD 60630) | 64 |
| 4.7 | (a) HRTEM micrograph, (b) SAED pattern and (c) magnified view of SAED pattern of CdSe revealed the [103] plane | 65 |
| 4.8 | Existence of fully occupied (box), fully unoccupied (arrows) and partially occupied (circle) atomic layers in [103] plane could be the reason of quenched diffraction peak | 65 |
| 4.9 | [002] plane showed very distinct intensity of x-ray diffraction consists of fully occupied atomic layers by only Se atoms (arrows) | 66 |
| 4.10 | [110] plane showed very distinct intensity of x-ray diffraction consists of fully occupied atomic layers by Cd and Se atoms (boxes) | 66 |
| 4.11 | (a) TOP-Se and TOP-Cd preparation apparatus set up and (b) dissolved aliquots in chloroform for UV-Vis and PL measurements | 67 |
| 4.12 | Temporal evolution of the first excitonic peak position within (a) 4, (b) 64 and (c) 169 hours of reaction at room temperature. The first excitonic peak red-shifted (d) upon 5 hours of 50 °C heating and maintained till (e) 24 hours after cooling down to room temperature | 68 |
| 4.13 | Temporal evolution of the PL property of CdSe QDs within (a) 4, (b) 169 hours (same PL was observed for 64 hours) of reaction at room temperature and (c) upon 5 hours of 50 °C heating (same PL was observed upon 24 hours of cooling) | 69 |
| 4.14 | High PL intensity of (a) organometallic-based QDs (64 hours of slow reaction), whereas very low PL intensity of (b) microemulsion-based QDs (2 hours of fast reaction) was observed. The intensity was normalized by absorbance at PL excitation wavelength of each sample | 70 |

| Figure No. | Title | Page |
|------------|---|------|
| 4.15 | (a) Broad XRD peaks of wurtzite CdSe QDs. Vertical lines indicate the possible Bragg reflections (JCPDS-ICDD 60630) | 73 |
| 4.16 | Basic structure of hexagonal P63mc CdSe crystal | 74 |
| 4.17 | Procedure of realistic cluster modelling | 75 |
| 4.18 | (From left) The front, side and rear view of optimized geometries of (a) (CdSe) ₆ , (b) (CdSe) ₁₃ , (c) (CdSe) ₁₆ , (d) (CdSe) ₂₆ and (e) (CdSe) ₃₂ | 76 |
| 4.19 | Calculated infrared spectra shows positive frequencies confirming a minimum energy structure of (a) (CdSe) ₆ , (b) (CdSe) ₁₃ , (c) (CdSe) ₁₆ , (d) (CdSe) ₂₆ and (e) (CdSe) ₃₂ clusters | 77 |
| 4.20 | Comparison of calculated transition oscillator strength (dashed lines) with experimental absorption spectra (solid lines) of (a) (CdSe) ₆ and (b) (CdSe) ₁₃ structures. Insets are magnified view of HOMO-LUMO transition at ~394 nm and ~410 nm respectively. The oscillator strength marked with “●” is the HOMO–LUMO transition | 79 |
| 4.21 | Comparison of calculated transition oscillator strength (dashed lines) with experimental absorption spectra (solid lines) of (a) (CdSe) ₁₆ and (b) (CdSe) ₂₆ structures. Insets are magnified view of HOMO-LUMO transition at ~462 nm and ~502 nm respectively. The oscillator strength marked with “●” is the HOMO–LUMO transition | 80 |
| 4.22 | Comparison of calculated transition oscillator strength (dashed lines) with experimental absorption spectra (solid lines) of (CdSe) ₃₂ structure. Inset is magnified view of HOMO-LUMO transition at ~650 nm; matched with the fitted $1S_{3/2} - 1S_e$ transition (Appendix B8) marked with “●” | 81 |
| 4.23 | (a) Optimized structure of (CdSe) ₆ which contains 3C Cadmium atomic sites made by (b) stacking of 6 trigonal pyramids which also the surface atoms that involve in ligand adsorption | 83 |

| Figure No. | Title | Page |
|-------------------|---|-------------|
| 4.24 | (a) Optimized structure of $(\text{CdSe})_{13}$ which contains 3C Cadmium atomic sites made by (b) stacking of 13 trigonal pyramids which also the surface atoms that involve in ligand adsorption | 83 |
| 4.25 | (a) Optimized structure of $(\text{CdSe})_{16}$ which contains 2C and 3C Cadmium atomic sites made by (b) stacking of 13 trigonal pyramids which also the surface atoms that involve in ligand adsorption | 84 |
| 4.26 | Cluster of $(\text{CdSe})_{26}$ which contains (a) surface 3C (trigonal pyramid) Cadmium atomic sites that involve in ligand adsorption, (b) interior 4C (tetrahedron) and (c) interior 5C (trigonal bipyramid) Cadmium atomic sites that do not involve in ligand adsorption | 84 |
| 4.27 | Cluster of $(\text{CdSe})_{32}$ which contains (a) surface 2C, (b) surface 3C (trigonal pyramid) and (c) surface 4C (tetrahedron) Cadmium atomic sites that involve in ligand adsorption and (d) interior 4C Cadmium atomic sites that do not involve in ligand adsorption | 83 |
| 4.28 | Optimized structure of N3 dye molecule | 85 |
| 4.29 | Comparisons of calculated transition oscillator strength (dashed lines) with experimental absorption spectra (solid curve) of N3 dye structure. The oscillator strength marked with “●” is the electron transition from HOMO-LUMO transition | 86 |
| 4.30 | Calculated infrared spectra shows positive frequencies confirming a minimum energy structure of N3 dye molecule | 87 |
| 4.31 | (a) Optimized structure of MAA. The calculated IR spectra (red curve) matched well with the experimental IR spectra (black curve); shows (b) C-O stretching, (c) O-H bending and (d) C=O stretching of $-\text{COOH}$ functional group and (e) $-\text{SH}$ stretching of mercaptan | 88 |

| Figure No. | Title | Page |
|-------------------|--|-------------|
| 4.32 | (a) Optimized structure of MPA. The calculated IR spectra (red curve) matched well with the experimental IR spectra (black curve); shows (b) C-O stretching, (c) O-H bending and (d) C=O stretching of –COOH functional group and (e) –SH stretching of mercaptan | 88 |
| 4.33 | (a) Optimized structure of MSA. The calculated IR spectra (red curve) matched well with the experimental IR spectra (black curve); shows (b) C-O stretching, (c) O-H bending and (d) C=O stretching of –COOH functional group and (e) –SH stretching of mercaptan | 89 |
| 4.34 | (a) Optimized structure of MBA. The calculated IR spectra (red curve) matched well with the experimental IR spectra (black curve); shows (b) C-O stretching, (c) O-H bending and (d) C=O stretching of –COOH functional group and (e) –SH stretching of mercaptan | 89 |
| 4.35 | Calculated Optimized structures of (a) (CdSe) ₁₃ –MAA, (b) (CdSe) ₁₃ –MBA, (c) (CdSe) ₁₃ –MPA and (d) (CdSe) ₁₃ –MSA conjugates | 92 |
| 4.36 | Calculated Infrared spectra of (a) (CdSe) ₁₃ –MAA, (b) (CdSe) ₁₃ –MBA, (c) (CdSe) ₁₃ –MPA and (d) (CdSe) ₁₃ –MSA conjugates show positive frequencies confirming minimum energy structures | 93 |
| 5.1 | (a) Schematic diagram of device structure of DSSC, QDSC with ligand and without ligand respectively and (b) energetic diagram showing exciton dissociation at sensitizer-MOS interface | 95 |
| 5.2 | Simulated absorption spectra of (a) N3 dye, (b) (CdSe) ₆ , (c) (CdSe) ₁₃ , (d) (CdSe) ₁₆ , and (e) (CdSe) ₂₆ , generated from energy calculations of DFT. Vertical lines are the calculated oscillator strengths at excitonic peak position of each fluorophore. | 97 |
| 5.3 | Absorption cross section of (CdSe) _x QDs with diameter of ~4 nm is predicted higher than that of N3 dye molecule | 98 |
| 5.4 | Off-set minimization could minimize the amount of energy lost during injection and increase the final conversion efficiency | 99 |

| Figure No. | Title | Page |
|------------|--|------|
| 5.5 | Shows calculated HOMO and LUMO energy levels of $(\text{CdSe})_6$, $(\text{CdSe})_{13}$, $(\text{CdSe})_{16}$ and $(\text{CdSe})_{26}$ clusters. Presence of multi-size CdSe QDs hinders efficient charge injections to photoelectrode in QDSCs | 100 |
| 5.6 | Uniform and uneven LUMO distributions at Cd and Se atoms made $(\text{CdSe})_6$ cluster is electronically unstable as observed from (a) front, (b) side and (c) rear view. Boxes show the LUMO density of Se atoms is smaller, compared to that of Cd atoms | 101 |
| 5.7 | Uniform and even LUMO distribution made $(\text{CdSe})_{13}$ cluster is electronically stable as observed from (a) front, (b) side and (c) rear view. 13 Cd atoms (arrows) are identified, possible for MSA ligand (inset) adsorption with overlapping wave function with $-\text{SH}$ functional group (circle) | 102 |
| 5.8 | Nonuniform and uneven LUMO distributions at Cd and Se atoms made $(\text{CdSe})_{16}$ cluster is electronically unstable as observed from (a) front, (b) side and (c) rear view. Boxes show Cd atoms without LUMO density which is not possible for MSA ligand adsorption with wave function overlapping | 102 |
| 5.9 | In $(\text{CdSe})_{26}$ LUMO density is only localized at Se atoms as observed from (a) front, (b) side and (c) rear view, denotes that MSA ligand adsorption with wave function overlapping is not possible | 103 |
| 5.10 | (a) Non-uniform and uneven LUMO distributions at Cd and Se atom make the $(\text{CdSe})_{32}$ cluster electronically unstable as observed from (a) front, (b) side and (c) rear view. Circles show Cd atoms without LUMO density and arrows marked the external Cd atoms | 103 |
| 5.11 | LUMO is extended to the anchoring hydrogen in $-\text{COOH}$ group of N3 dye molecule as observed from (a) front, (b) side and (c) rear view | 103 |
| 5.12 | (a) Four anchoring hydrogen in carboxylic functional groups (circles) are observed in the optimized ground state structure. (b) The distance between the nearest LUMO site to the anchoring hydrogen is measured in the emitting state of N3 dye, which generated using TDDFT calculations | 105 |

| Figure No. | Title | Page |
|------------|---|------|
| 5.13 | The LUMO of (a) MAA, (b) MBA, (c) MPA and (d) MSA, reveal the distance of the nearest LUMO site to the anchoring hydrogen in $-\text{COOH}$ (dashed circle) and $-\text{SH}$ (solid circle) functional groups. Insets are optimized structure of the ligands | 106 |
| 5.14 | (a) $(\text{CdSe})_{13}$ -MAA and (b) $(\text{CdSe})_{13}$ -MPA conjugates from front and rear view. Boxes show only small portion of LUMO on MAA and MPA molecules denote inefficient electron injection from $(\text{CdSe})_{13}$ to both ligands | 108 |
| 5.15 | (a) Properly aligned energy level of QDSC components favors electron regeneration from electrolyte to $\text{HOMO}_{\text{CdSe}}$. (b) Higher energy level of E^o of IonLic BMII than that of $\text{LUMO}_{\text{TiO}_2}$ prohibits electron injection from TiO_2 to electrolyte, thus, electron regeneration in $\text{HOMO}_{\text{CdSe}}$ is retarded | 110 |
| 5.16 | Optimized structure of 1-butyl-3-methylimidazolium iodide ionic liquid (IonLic BMII) in gas phase at B3LYP/lanl2dz level of DFT. The optimized parameters and validation procedure are presented in Appendix K | 110 |
| 5.17 | Born-Haber thermodynamic cycle for standard redox potential calculations | 112 |
| 5.18 | (a) Energy level misalignment, i.e., $E^o > \text{LUMO}_{\text{TiO}_2}$ preventing electron regeneration of N719 dye. (b) E^o shift due to addition of I_2 redox couple, TBP and GuNCS co-additives is speculated; could favor N3 dye reduction | 113 |
| 6.1 | The PL of bare CdSe QDs and CdSe QDs- TiO_2 conjugate originates from radiative recombination of excited state electron from $\text{LUMO}_{\text{CdSe}}$ to $\text{HOMO}_{\text{CdSe}}$. The number of electron recombination in the conjugate is lesser than that of the bare QDs due to electron injections to TiO_2 ; that leads to quenching of PL intensity | 115 |
| 6.2 | FESEM micrographs shows mesoporous TiO_2 layer (thickness $\sim 12 \mu\text{m}$) on FTO glass as observed at (a) 3 000 and (b) 25 000 times magnification | 116 |

| Figure No. | Title | Page |
|------------|--|------|
| 6.3 | Absorption spectra of (a) as synthesized CdSe QDs dissolved in acetonitrile, (b) bare TiO ₂ film, (c) CdSe–TiO ₂ (DA), (d) CdSe–MSA–TiO ₂ and (e) CdSe–MPA–TiO ₂ . The size of the cluster estimated from the absorption spectra of the bare CdSe QDs to be ~3.69 nm; assigned to (CdSe) ₃₂ cluster | 117 |
| 6.4 | (a) PL of as prepared CdSe QDs solution in acetonitrile. Electron injection from CdSe QDs to TiO ₂ was determined by a quenched PL intensity of (b) CdSe–MPA–TiO ₂ , (c) CdSe–MSA–TiO ₂ and (d) CdSe–TiO ₂ conjugate. The PL spectra have been normalized based on their individual absorbance intensity for a fair comparison | 118 |
| 6.5 | Hindered electron injection from CdSe QDs to TiO ₂ due to inefficient electron channelling via MSA ligand (LUMO _{MSA} > LUMO _{CdSe}). The same energy level misalignment was observed for MPA-based conjugate. Energy levels were calculated and presented in chapter 5, section 5.4.2.3 | 118 |
| 6.6 | (a) Bare TiO ₂ nanowires before CdSe QDs attachment and (b) successful CdSe QDs attachment onto TiO ₂ in a form of core–shell nanowire by the SILAR technique as observed using transmission electron microscopy | 119 |
| 6.7 | XRD pattern of (a) bare anatase TiO ₂ nanowire film on FTO (JCPDS 84-1286) and (b) CdSe QDs conjugated TiO ₂ nanowire on FTO | 120 |
| 6.8 | (a) Similar absorption curve of bare CdSe and CdSe–conjugated TiO ₂ showed a successful sensitization | 121 |
| 6.9 | Quenched PL intensity in the core-shell nanowire curve (dashed curve) shows a successful electron injection from CdSe shell to TiO ₂ core | 122 |
| 6.10 | Excited state electron mapping using quantum mechanical calculations shows (a) even and uniformly distributed excited state electron at surface atoms of (CdSe) ₁₃ and (b) localized excited state electron in the core atoms of (CdSe) ₃₂ cluster; which used in QD–TiO ₂ conjugation using SILAR and DA procedure respectively | 122 |

| Figure No. | Title | Page |
|-------------------|--|-------------|
| 6.11 | CdSe QDs attachment onto TNRs via immersion of FTO in TOP-Se and TOP-Cd solution within (a) 4 hours, (b) 24 hours and (c) 168 hours. (d) Bare TNRs layer on FTO glass | 123 |
| 6.12 | XRD pattern of CdSe QDs conjugated TNRs on FTO. Vertical lines denote the standard diffraction data of rutile TiO ₂ (JCPDS 88-1175) | 124 |
| 6.13 | FESEM micrographs shows (a) bare TNRs grown on FTO (diameter of rod ~100 nm and length ~1 μ m) and (b) CdSe QDs coated TNRs at 30 000 magnifications from top view (top) and cross-section view (bottom). Presence of CdSe QDs is unobservable | 124 |
| 6.14 | Uneven and small adsorption area of CdSe QDs on TNRs-FTO upon immersion for 4 hours as indicated by the dotted area | 125 |
| 6.15 | Absorption spectra of (a) CdSe QDs aliquots at 4 hours of reaction time, (b) bare TNRs – FTO and (c) TNRs – FTO immersed in TOP CdSe QDs aliquots for 4 hours | 125 |
| 6.16 | (a) PL of CdSe QDs aliquots upon 4 hours of reaction time, (b) successful electron injection from CdSe QDs to TNRs determined by drastic quenched of PL intensity and (c) upon exposure to air for 3 days, the PL intensity increased | 126 |
| 6.17 | Absorption spectra of (a) fresh TNRs – FTO immersed in TOP CdSe QDs aliquots for 4 hours and (b) upon 3 days exposure to air | 127 |
| 6.18 | Absorption spectra of (a) CdSe QDs aliquots at 24 hours of reaction time, (b) bare TNRs – FTO and (c) TNRs – FTO immersed in TOP CdSe QDs aliquots for 24 hours | 128 |
| 6.19 | Wide and uneven coverage of CdSe QDs adsorption within 24 hours of TNRs – FTO immersion | 128 |
| 6.20 | (a) PL of CdSe QDs aliquots upon 24 hours of reaction time, (b) successful electron injection from CdSe QDs to TNRs determined by quenched of PL intensity | 129 |
| 6.21 | Wide and even coverage of CdSe QDs adsorption within 168 hours of TNRs – FTO immersion | 129 |

CHAPTER 1

INTRODUCTION

1.1 BACKGROUND

The quantum dots (QDs), the semiconducting nanocrystals of size less than their exciton Bohr radius with size-dependent opto-electronic properties, have been fascinating materials to scientists and engineers for nearly two decades. This fascination stems from two reasons: firstly, QDs are midway between molecules and crystals thereby giving opportunities to understand the evolution of properties of bulk materials compared to their molecules. Secondly, their size dependent opto-electronic properties make them promising candidates for a diverse range of applications. Figure 1.1 shows that when a bulk semiconductor is reduced to the size of QDs, one can observe that the density of states (DoS) of QDs is very similar to that of atoms, which enable them to be called artificial atoms (Alivisatos, 1996a).

Applications of QDs, where semiconductor physics meets nanotechnology, are now envisaged in diverse areas such as opto-electronics (Su et al., 2013), healthcare (Li et al., 2013), computation (Dietl et al., 2000), PVs (Rühle et al., 2010), and advanced electronics (Hai et al., 2013). The principle attraction in the use of QDs for PVs is related to the thermodynamic limit of the energy conversion efficiency of solar cells. Shockley and Queisser (1961) have calculated the thermodynamic limit of conversion efficiency for solar cells to be 32%. This limit arises from the difference between the energy absorbed by the photoactive semiconductor and its bandgap. As the electron injection or separation occurs only from the bottom of the conduction band, the above difference in energy is lost as heat through excitation of the lattice vibrations, otherwise called phonon relaxation (see Figure 1.2.a). In other words, the electrons are “cooled” by transferring the difference in energy to the lattice.

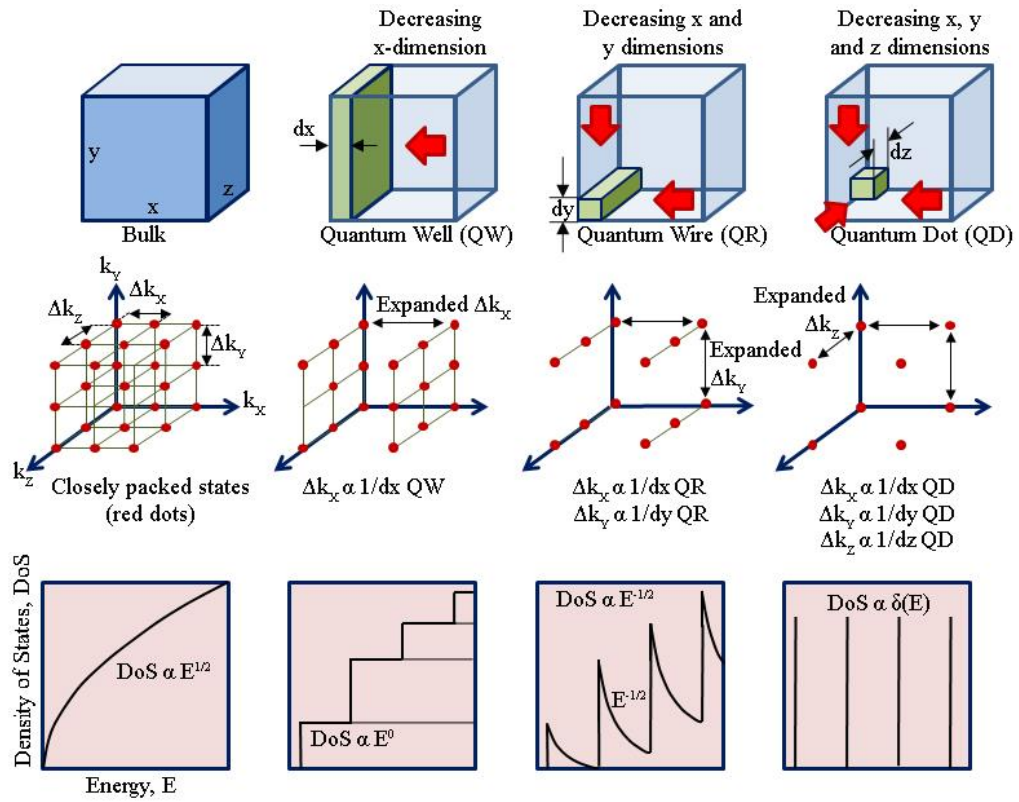


Figure 1.1: The series of events in the electron DoS when a bulk semiconductor is reduced to the size of QDs

Source: Redrawn from Hoogland (2008)

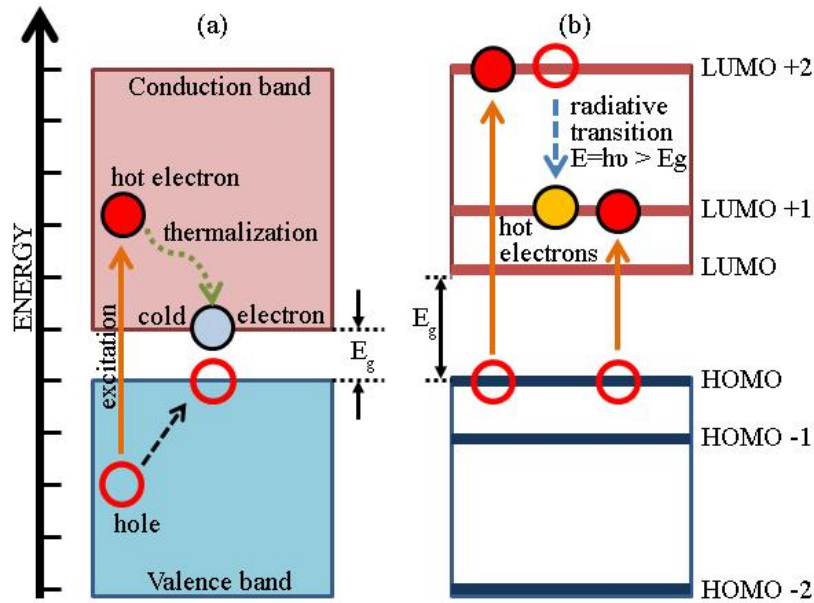


Figure 1.2: Energetic diagram of (a) thermalization in bulk structure and (b) multi-exciton generation (MEG) in quantum wells and dots

Adapted from: Nozik (2001a and 2002b)

1.2 PROBLEM STATEMENT

The QDs are shown to generate more than one electron per absorption of single photon of sufficient energy (Luque, 2007) – a phenomenon known as multi exciton generation (MEG) (see Figure 1.2.b). Utilization of this phenomenon in solar cells would result in increased photovoltaic conversion efficiency, theoretically up to 60%. Three device architectures are considered to capitalize the salient features of QDs in solar cells, viz., (i) Schottky junction solar cells, in which the PV effect occurs at a metal – QDs interface; (ii) organic solar cells, in which the PV effect occurs at a QDs – polymer interface; and (iii) QDSCs, in which the PV effect occurs at the interface between QDs conjugated wide band gap MOS and redox electrolyte. Among them QDSCs gained much popularity due to their relatively simple structure and similarity with another solar cell, called DSSCs, in which dye molecules replace QDs.

CHAPTER 3

MATERIALS AND METHOD

3.1 RESEARCH METHODOLOGY

This chapter explains the methodology adopted in this research. Basic principles of the instruments used in this research, an overview of the instrumentation, possible errors, and sample preparation methods are detailed in this chapter.

Figure 3.1 shows the details of the research methodology. Correlation between QDs structure and the effect to the electron injection properties of QDSC was established using experimental and theoretical approaches. Structures of synthesized QDs were modelled based on crystal structure obtained by XRD and TEM; due to lack of information about their exact geometries. Series of calculations were carried out for structure optimization and realistic cluster model validation. Properties of the models were calculated i.e, (i) excited state electron mapping (LUMO map); (ii) absorption cross sections of single cluster (α_A) and (iii) excited state and ground state energy levels; which are not experimentally feasible. Concurrently, models of dye, ligands and electrolyte were also optimized and validated. A thorough cell efficiency analysis was made in terms of the stated properties based on experimentally established QDSCs and DSSCs; fabricated using these components. Properties of QDs–ligand conjugates were also examined, i.e., adsorption energy and electron channelling efficiency; nonetheless effect of redox potential of electrolyte was also studied. To strengthen the findings, electron injection efficiency from QDs to MOS was studied. QDs–MOS conjugates were fabricated using five methods viz., SILAR, DA, LA, CBD and organo-metallic routes; utilizing CdSe QDs with structure and properties similar to the modelled ones.

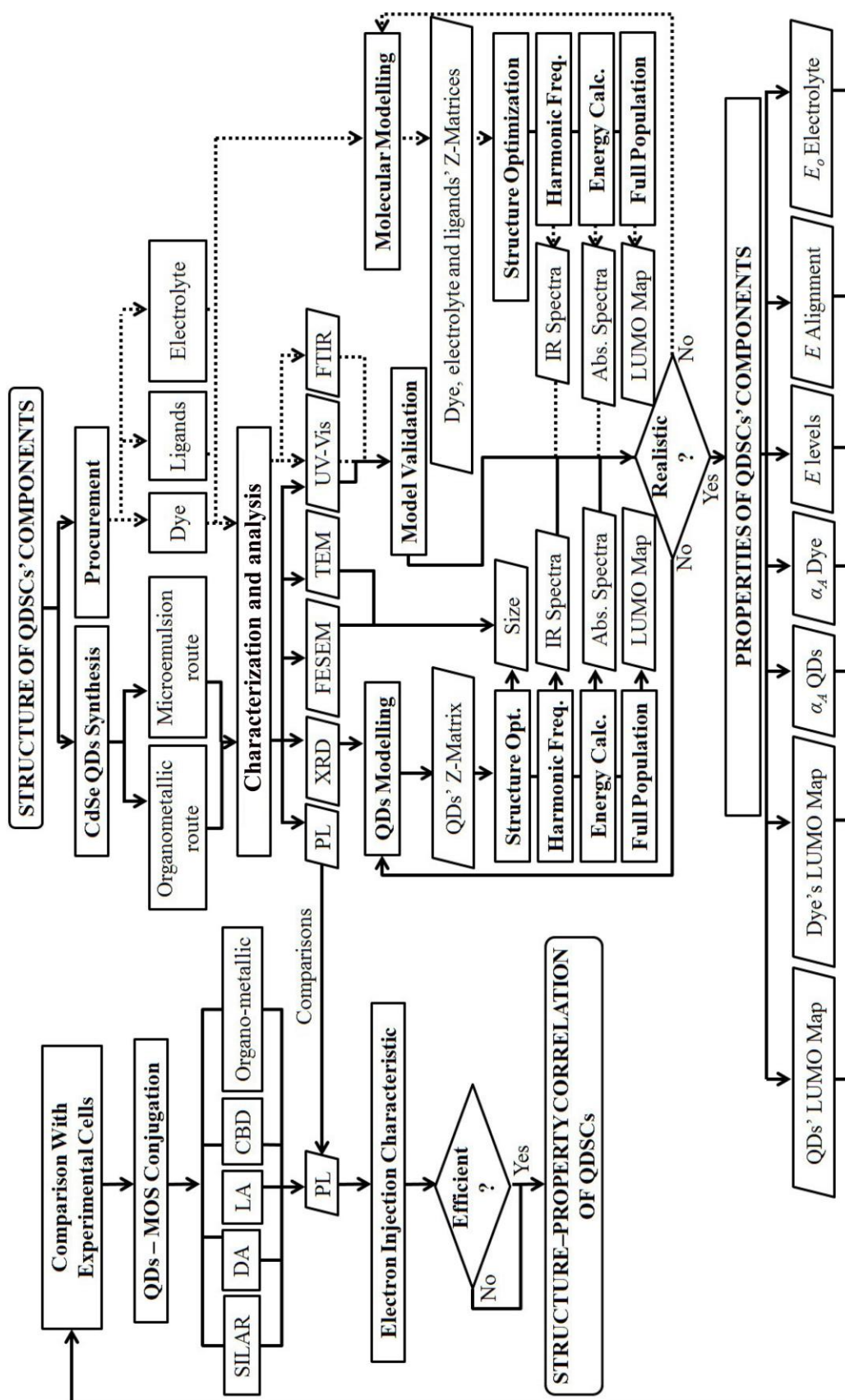


Figure 3.1: Flow of research methodology

3.2 CdSe QUANTUM DOTS SYNTHESIS AND CHARACTERIZATION

3.2.1 Microemulsion Synthesis Procedure

Non-ionic food grade surfactant sucrose ester S1670 was purchased from Mitsubishi Kagaku Food, 1-heptanol was supplied by Merck and deionized water (Purelab Prima Elga, 18.2 M Ω electrical resistivity) was used throughout sample preparations. Microemulsion phase was determined by varying 63 compositions of the components at 37 °C. All samples were prepared by mixing directly in glass vials by weight percentage (wt%) of each component and kept in water bath at 37 °C overnight to reach equilibrium state. Phase determination was done using Nikon e-clipse 2000 polarizing optical microscope with Nikon D5000 camera and heating stage attachments. Three phases were observed i.e., (i) lamellar phase liquid crystal, (ii) microemulsion and (iii) emulsion.

Lamellar phase lyotropic liquid crystals showed birefringency; easily observed compared to the isotropic microemulsion and emulsion phases that showed continuous black image by polarization of light. Microemulsion and emulsion phases were distinguished based on their physical appearance. Microemulsion phase appeared in a form of clear and thick solution; whereas emulsion phase appeared in a form of turbid and thick solution. The size of water droplets in emulsion phase is measureable under the microscope without polarization of light. Microscope images and ternary phase diagram of microemulsion region are presented in Appendix A (Figure A1-A3 and A4 respectively). The type of microemulsions was determined using conductivity test. Water in oil (w/o) type of microemulsions has conductivity lower than 1 μ S/cm; whereas oil in water (o/w) microemulsion has higher than the specified value (Nesamony et al., 2005). Conductivity measurement is presented in Appendix A (Table A1).

For CdSe QDs synthesis, ~0.25 M Sodium Selenosulphate as Se precursor was prepared by an overnight reflux process of 5 g Se powder (ACS Across) and 15 g Sodium Sulfite anhydrous (Fluka) in 200 ml deionized water at 98 °C with constant stirring. The solution were cooled down to room temperature; filtered away undissolved